Fluid–structure modelling for material deformation during cavitation bubble collapse

Prasanta Sarkar, Giovanni Ghigliotti, Jean-Pierre Franc, Fivel Marc

Fluid-structure modelling for material deformation during cavitation bubble collapse

Prasanta Sarkar [a,*], Giovanni Ghigliotti[a], Jean-Pierre Franc[a], Marc Fivel[b]

[a] *Univ. Grenoble Alpes, CNRS, Grenoble INP, LEGI, 38000 Grenoble, France*
[b] *Univ. Grenoble Alpes, CNRS, Grenoble INP, SIMaP, 38000 Grenoble, France*

Abstract

The dynamics of cavitation bubbles and their interaction with solids has been studied for long, mostly on the macro-scale of sheet and vortex cavitation. Erosion takes place on small, concentrated areas of solid walls exposed to cavitation. One-way fluid structure interaction (FSI), in which the feedback of material deformation on the fluid is not considered, provides an adequate understanding of the underlying mechanism. However, in practical applications the solid material motion and deformation can significantly affect the bubble dynamics. This will, in principle, alter the structural loading, stresses and erosion in the solid. In this paper, we will report comparisons of one-way and two-way coupled FSI modelling using our finite volume based fluid solver YALES2 [1] and finite element based solid solver Cast3M [2]. In two-way FSI coupling, the feedback of the solid wall deformation is considered in the fluid domain. To do so, we develop a compressible fluid solver with Arbitrary Lagrangian-Eulerian formulation to equip it with moving mesh capabilities in order to maintain a continuous fluid-solid domain. We present results using a *step-wise coupling approach* for two-way FSI and analyse the effects due to structural response on bubble dynamics and damping of impact pressures by different materials. Finally, we discuss our understanding on the need for one-way and two-way FSI modelling based on structural characteristics which can significantly affect the material erosion by nearby cavitation bubbles.

Keywords: cavitation ; cavitation erosion ; fluid-structure interaction ; one-way coupling ; two-way coupling

1. Introduction

Violent collapse of bubbles near surfaces has generated interest in many scientific fields including cavitation, shock wave and laser-lithotripsy. In cavitation, solid

∗. Corresponding author.
1. http ://yales2.coria-cfd.fr
2. http ://www-cast3m.cea.fr

surface erosion or damage is caused when bubbles collapse in the vicinity of the solid surface. In hydrodynamics, cavitation regimes comprising many bubbles are often encountered on the low pressure sides of the blades of hydraulic machines. Consequences are numerous : modification of the flow that can lead to dramatic drop in performance, surface erosion and structural damages in addition to vibrations. The cavitation bubbles usually collapse near the point of inception or travel downstream with the flow before they collapse. When close enough to a solid wall these collapses are usually associated with high-speed liquid micro-jet formation (Blake and Gibson (1987)) and emission of shock waves. In key applications, unexpected damages and early replacement of the machines can result in huge economic cost. On the brighter side, cavitation erosion is increasingly considered as a tool for beneficial use as well, such as in shock wave lithotripsy, drug-delivery, microchip cleaning and microfluidics (Lauterborn and Vogel (2013)).

Silverrad (1912) was one of the first to report erosion on the propeller of large cruise boats. Such erosive damages on the low pressure zones generated by the high rotation speed on the propeller blades raised experimental interest in the study of cavitation. Since then many studies dealing with problems from bubble dynamics to material testing have been pursued like Plesset and Chapman (1971), Lauterborn and Ohl (1997), Tong et al. (1999)), Franc (2009), all aiming towards a better understanding of cavitation erosion. Although the early work focused mostly on theoretical and experimental findings, numerical techniques and improved computational resources have added to the understanding of bubble-wall interactions (Best and Kucera (1992), Wang and Blake (2010), Popinet and Zaleski (2002),Tinguely (2013)). Overall, the problem is a difficult one as it involves complicated flow phenomena combined with material characteristics of the solid wall.

Many cavitation erosion models have been proposed based on energy conservation and focusing of the potential energy of vapor cavities in space and time transferred on the material surface. Some models like Fortes-Patella et al. (2004) based on the physical scenario of collapsing vapor structures propose that the final material damage results from the interaction of pressure waves and neighbouring solid surface. Dular (2006) suggested an erosion model from collapse of cavitation cloud and emission of shock wave that attenuates as it travels towards the solid surface. The shock wave excites the individual bubbles near the solid surface and the final damage pits are formed from the high velocity liquid jet impacting the solid surface. Material deformation and pitting from cavitation bubble collapse has also gained a lot of interest in the recent years (Roy et al. (2015a), Pöhl et al. (2015), Fivel et al. (2015)). A Fluid-structure Interaction (FSI) study provides insight into different dynamical features of fluid and solid mechanics, connecting the links between cavitation loads and surface deformation (Tijsseling and Vardy (2005), Chahine and Hsiao (2015), Kumar and Wurm (2015), Gong et al. (2016), Paquette (2017), Joshi et al. (2019)).

Despite more than a century of research, a thorough description of the physical processes of cavitation erosion is still not available. Emphasis has been laid on preventing the initiation of cavitation and where not possible to prevent, minimise the erosive damages. However, an effective prevention strategy and further beneficial exploitation necessitates a deeper understanding of the fundamental physical phenomena in both fluids and solids. This understanding has been pursued in this research with the simplest form of cavitation, the single bubble.

In this paper we will present comparisons of one-way and two-way coupled FSI model of bubble collapse near solid walls. A one-way FSI coupling between fluid and solid domains is unidirectional, with surface pressures passed from fluid to solid in order to determine material deformation. A two-way coupling, on the other hand, is bidirectional in terms of information exchange between the two physical domains. The surface pressure and deformation are passed to solid and fluid domains respectively. To do so, we will introduce a *step-wise coupling* for FSI between Computational Fluid Dynamics *(CFD)* and Computational Solid Mechanics *(CSM)*. The focus in this paper is to demonstrate a strong fluid-solid step-wise FSI coupling between CFD solver YALES2 and CSM solver Cast3M, along with the implementation of Arbitrary Lagrangian-Eulerian formulation in a predictor-corrector scheme of compressible *Navier-Stokes* equations. Such formulation and coupling methodology for cavitation bubble collapse, in our opinion, is unique and has never been done before.

The paper is structured as follows : Section 2 introduces the development of the cavitation solver with Arbitrary Lagrangian-Eulerian formulation ; Section 3 discusses the methodology for *step-wise coupling* FSI ; Section 4 discusses the comparisons of one-way vs two-way FSI for bubble collapse and Section 5 will discuss major conclusions.

2. Numerical solvers

The numerical simulation of accurate two-way coupled FSI problem requires to account for the distortion of both fluid and solid computational domains. While *CSM* is usually dealt with by using a Lagrangian framework, in CFD the standard is to use Eulerian framework. Therefore to match the Lagrangian solid domain in our CSM solver, a compressible cavitation solver in CFD needs to be developed in a numerical framework that not only allows to delineate fluid phase interfaces accurately, but can also provide continuous fluid-structure domain with moving boundaries. Neither the Eulerian nor the Lagrangian formulations are optimal for the entire domain due to their respective limitations. The Eulerian formulation widely used in fluid mechanics has a computational mesh fixed in space, with the continuum (materials modeled as a continuous mass) moving with respect to the mesh. Although the continuum motion relative to the mesh can be handled easily with some complexity in resolving the transport of the material, it cannot

resolve a deforming domain since the mesh is fixed in space. The Lagrangian formulation mainly used in solid mechanics is the one where the mesh moves with the material, allowing ease in resolving material interfaces accurately but the nodal positions need to be updated at every time step in order to conform with the solid body dynamics. For such cases, the Arbitrary Lagrangian Eulerian (ALE) formulation is quite attractive and has been implemented in our solver algorithm in YALES2. ALE combines the best features of both the approaches and allows for the movement of nodes of the computational mesh with the continuum in normal Lagrangian manner or to be held fixed in Eulerian manner or, more importantly, in any intermediate way. An ALE-equipped fluid mesh can conform to the Lagrangian mesh deformation of the solid at the fluid-structure interface which is a convenient framework for the FSI problem of bubble collapse. Since the ALE mesh moves relative to the material in the fluid domain, similar transport terms to the existing Eulerian formulation of the compressible cavitation solver exist. Therefore, implementation of ALE formulation will benefit from many of the existing algorithms. Such ALE equipped solver can be used to model compressible simulations of realistic complex geometries like rotor-stator stages in aeronautics or hydraulic turbines, deformable walls in bio-mechanical flows.

2.1. Arbitrary Lagrangian-Eulerian framework

The motion of individual nodes of a computational mesh with its associated material particle motion is shown in fig. 1 for Eulerian, Lagrangian and ALE frameworks. The original development of ALE is credited to, among others, Hirt

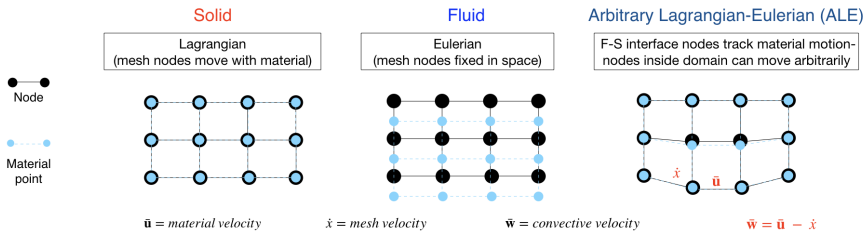

FIGURE 1: 2D Eulerian, Lagrangian and ALE mesh node motion with associated material particle motion.

et al. (1974) and an in-depth introduction to the mathematical framework is given in Donea et al. (2004). In the ALE formulation, the individual nodes can be moved in some specified way with respect to the material particle, thus offering more freedom in moving the computational mesh. The fundamental relationship between the material, referential time derivative and spatial gradients obtained by domain mapping between the material coordinates $\underline{X}$, spatial coordinates $\underline{x}$

and ALE referential coordinates $\underline{\chi}$ can be expressed as :

$$\left.\frac{\partial f}{\partial t}\right|_{\underline{X}} = \left.\frac{\partial f}{\partial t}\right|_{\underline{\chi}} + \left.\frac{\partial f}{\partial t}\right|_{\underline{x}} \cdot \underline{w} = \left.\frac{\partial f}{\partial t}\right|_{\underline{\chi}} + \underline{w} \cdot \nabla f \tag{1}$$

Here $\underline{w}$ is the convective velocity, defined as the relative velocity between the material velocity $\underline{u}$ and the mesh velocity $\underline{\dot{x}}$ such that $\underline{w} = \underline{u} - \underline{\dot{x}}$ and t is the time. Equation (1) represents the material derivative of f which is expressed as its local derivative in a fixed reference coordinate $\underline{\chi}$ plus a convective term $\underline{w}$ between the material and the reference spatial coordinates.

2.2. Compressible ALE solver

The ALE form of the compressible *Navier-Stokes* equations resolved in our CFD simulations is obtained by replacing the material velocity $\underline{u}$ by the convective velocity $\underline{w} = \underline{u} - \underline{\dot{x}}$ shown in eq. (2) & (3).

$$\frac{\partial \rho}{\partial t} + \nabla \cdot (\rho \underline{w}) = 0 \tag{2}$$

$$\frac{\partial \rho \underline{u}}{\partial t} + \nabla \cdot (\rho \underline{u} \otimes \underline{w}) = -\nabla p + \nabla \cdot \underline{\underline{\tau}} \tag{3}$$

Here ρ is the fluid density, p is the pressure, $\underline{\underline{\tau}}$ is the viscous stress tensor, t is the time, $(\nabla\cdot)$ is the divergence operator. The right-hand side of the equations has a form similar to the classical Eulerian form of *Navier-Stokes* equations whereas the mesh movement is reflected on the left-hand side of the governing equations. Setting $\underline{w} = 0$ (*i.e.* $\underline{\dot{x}} = \underline{u}$) gives the classical Lagrangian description whereas $\underline{w} = \underline{u}$ (*i.e.* $\underline{\dot{x}} = 0$) recovers the Eulerian description. The temporal scheme has to be recast in an ALE formulation with prescribed mesh movement at each sub-step of the time integration scheme to satisfy the geometry conservation law as well as numerical stability conditions. Geometry conservation law states that, independently of the mesh motion, the numerical scheme has to preserve the state of a uniform flow. The CFL and CFL_{acou} are then expressed in terms of the convective velocity $\underline{w}$, where Δt is the given time step and Δx is the mesh size.

$$CFL = |\underline{w}| \frac{\Delta t}{\Delta x} \tag{4}$$

$$CFL_{acou} = |\underline{w} + c| \frac{\Delta t}{\Delta x} \tag{5}$$

A characteristic splitting of the *Navier-Stokes* equations in ALE form in eq. (2) & (3) is outlined to achieve the fractional step method of time advancement (Moureau et al. (2007)). Equations (6) & (7) are solved for $\phi \in (\rho, \underline{m})$ in the prediction step with the convective velocity $\underline{\tilde{w}} = \underline{\tilde{u}} - \underline{\dot{x}}$ and $\underline{m} = \rho \underline{u}$ is the momentum in the set of conservative variables. In our numerical simulations, the energy equation

is not solved as the fluid is assumed to be barotropic, meaning the pressure is a function of density only. The mesh velocity $\underline{\dot{x}}$ can be determined explicitly or implicitly by solving an equation for the node displacement for specific boundary conditions.

$$\frac{\rho^\star - \rho^n}{\Delta t} + \nabla \cdot (\tilde{\rho}\underline{\tilde{w}}) - (\tilde{\rho} - \rho^n)\,\nabla \cdot \underline{\tilde{w}} = 0 \tag{6}$$

$$\frac{\underline{m}^\star - \underline{m}^n}{\Delta t} + \nabla \cdot (\underline{\tilde{m}} \otimes \underline{\tilde{w}}) - (\underline{\tilde{m}} - \underline{m}^n)\,\nabla \cdot \underline{\tilde{w}} = -\nabla p^n + \nabla \cdot \underline{\underline{\tau}}^n \tag{7}$$

For $\phi \in (\rho, \underline{m})$ in the prediction step, ϕ^n is the value of ϕ before time advancement, $\phi^\star$ is the value computed at the end of the prediction step and $\tilde{\phi}$ is the value computed at different steps of the temporal scheme with the pressure and diffusion being explicit contributions. The computational mesh reaches the final position of the time step at the end of the prediction step and a fixed mesh exists at this stage. The time integration is carried out with TFV4A (Kraushaar (2011)) scheme with the mesh being displaced only during the prediction step. The TFV4A scheme is developed by blending the low storage, explicit, fourth-order Runge-Kutta with a Lax-Wendroff-type scheme, allowing the in-built numerical diffusion in the temporal scheme to be adjusted. The spatial discretization is carried out by the fourth-order centered scheme (Malandain (2013)) and a non-linear artificial viscosity μ_{artif} in eq. (8) (Cook and Cabot (2004)) is used to stabilize non-physical, spurious oscillations. Here C_μ is the artificial viscosity constant, r is the artificial viscosity order, Δx is the mesh spacing and $\overline{|\ |}$ is the Gaussian filter applied. Furthermore in order to stabilize numerical simulations, a high order filtering based on volume-weighted averaging with a Gaussian-type smoothing has been applied on the pressure and density field after every specified number of iterations.

$$\mu_{artif} = C_\mu \rho\,(\Delta x)^r \overline{\left|\frac{\partial^r u}{\partial x^r}\right|} \tag{8}$$

The equation of state is used at the end of the prediction step to determine the intermediate pressure p^*. The algorithm solves for an intermediate speed of sound c^* computed from the advected ρ^* and p^*. The Helmholtz eq. (9) is solved over this fixed mesh with BiCGSTAB2 (Vantieghem (2011)) linear solver for the pressure variation $\delta p = p^{n+1} - p^\star$. The pressure variation δp is used to correct the conserved variables $\phi \in (\rho, \underline{m})$ in the correction step with eq. (10) & (11).

$$\begin{aligned}\nabla \cdot \nabla \left(p^{n+1} - p^\star\right) - \nabla \cdot \frac{\underline{w}^*}{(c^*)^2 \Delta t}\left(p^{n+1} - p^\star\right) - \frac{p^{n+1} - p^\star}{(c^*)^2 \Delta t^2} \\ = \nabla \cdot \nabla \left(p^n - p^\star\right) + \frac{\rho^\star - \rho^n}{\Delta t^2} + \frac{1}{\Delta t}\nabla \cdot (\rho^\star \underline{w}^\star)\end{aligned} \tag{9}$$

$$\frac{\rho^{n+1} - \rho^\star}{\Delta t} - \frac{1}{(c^*)^2}\frac{\delta p}{\Delta t} = 0 \tag{10}$$

$$\frac{\underline{m}^{n+1} - \underline{m}^{\star}}{\Delta t} - \frac{\underline{w}^{*}}{(c^{*})^{2}} \frac{\delta p}{\Delta t} = -\nabla (\delta p) \tag{11}$$

The equation of state is solved again at the end of the correction step to obtain a consistent $p^{(n+1)_c}$ and ρ^{n+1} at the end of the time step in the algorithm. A schematic of the compressible ALE solver algorithm is shown in fig. 2.

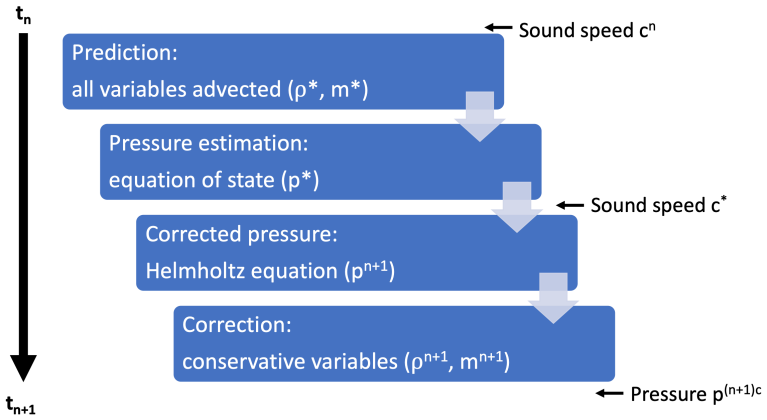

FIGURE 2: Compressible ALE solver's prediction-correction algorithm

The time integration in TFV4A is coupled with movement of mesh nodes and advancement of control volume in the prediction step. The convective flux $\underline{\tilde{w}} = \underline{\tilde{u}} - \underline{\dot{x}}$ has to be determined with the displaced control volume at each step of time integration. A classical time integration between t^n and t^{n+1} with a time step Δt for the transport term is in eq. (12) where RHS contains the viscous fluxes and pressure gradients.

$$\int_{t^n}^{t^{n+1}} \frac{\partial}{\partial t} \int_{\Omega(t)} \phi \partial\Omega \, dt + \int_{t^n}^{t^{n+1}} \int_{\Omega(t)} \nabla \cdot (\phi(\underline{u} - \underline{\dot{x}}))d\Omega \, dt = RHS \tag{12}$$

The sub-step of the time integration at $t^i = t^n + \Upsilon_i \Delta t$, for a classical fourth order Runge-Kutta scheme with coefficient $\Upsilon_i = [1/4, 1/3, 1/2, 1]$ is shown in eq. (13).

$$\begin{aligned} &\phi^n = \phi^0, \\ &\phi^i = \phi^n \frac{\Omega^n}{\Omega^i} - \Upsilon_i \frac{\Delta t}{\Omega_i} \int_{\Omega(t)} \nabla \cdot (\phi^{i-1}(\underline{u}^{i-1} - \underline{\dot{x}}^{n+1}))d\Omega, \text{ for } i = 1, 2, 3, 4 \\ &\phi^* = \phi^4 \end{aligned} \tag{13}$$

Here, ϕ^* is the predicted variable field, Ω^n is the nodal volume V_{node} at time t^n and Ω^i is V_{node} at time t^i. The mesh movement coefficient (Chnafa et al. (2014)) at each sub-step of the time integration has been derived in such a way that the numerical scheme satisfies a discrete geometry conservation law as in eq. (14) :

$$\Omega^i - \Omega^n = -\Upsilon_i \Delta t \int_{\Omega(t)} \nabla \cdot \underline{\dot{x}}^{n+1} d\Omega, \text{ for } i = 1, 2, 3, 4 \tag{14}$$

As per our knowledge, the characteristics-based fractional step method for compressible *Navier-Stokes* equation in ALE form has never been presented before. Such novel semi-implicit time integration for compressible flows with ALE alleviates the limitations encountered by explicit solvers at small acoustic CFL and at low-Mach numbers for moving boundary and fluid-structure interaction problems.

The two-phase cavitating flow is modelled with the homogenous mixture model, which assumes a homogenous mixture of liquid and vapor in the two phase region. The cavitating flow is treated as a single fluid, consisting of mixture of two fluids of varying density. The vapor volume fraction in each control volume is defined as $\alpha = \Omega_v/\Omega$, where Ω_v is the vapor volume in a control volume Ω. The volume average density in each control volume is calculated as a linear combination of vapor density ρ_v and liquid density ρ_l.

$$\rho = \alpha\rho_v + (1-\alpha)\,\rho_l \tag{15}$$

The fluid in our simulation is assumed to exist in two different phases defined by the respective equations of state which are barotropic, meaning that the pressure is a function of the fluid density only. One phase is the pure liquid water with vapor volume fraction $\alpha = 0$, modelled by the Tait's equation of state given in eq. 16. Another is the two-phase liquid-vapor homogenous mixture with $0 < \alpha < 1$ modelled by following an isentropic path in the phase diagram proposed by Egerer et al. (2013) in eq. 16. The two-phase liquid-vapor mixture is separated from the pure liquid phase by the saturation liquid density $\rho_{sat,l}$. The model constants used in the equations of state is given in table 1.

$$p = \begin{cases} (p_{sat} + B)\left(\frac{\rho}{\rho_{sat,l}}\right)^N - B & , \text{ if } \alpha = 0 \\ p_{sat} + C\left(\frac{1}{\rho_{sat,l}} - \frac{1}{\rho}\right) & , \text{ if } 0 < \alpha < 1 \end{cases} \tag{16}$$

For the pure liquid phase with $\alpha = 0$, a consistent speed of sound c given in eq.

Property	Value	Unit
$\rho_{sat,l}$	998.1618	kg/m^3
$\rho_{sat,v}$	0.01731	kg/m^3
p_{sat}	2340	Pa
B	3.078×10^8	Pa
C	1468.54	$Pa \cdot kg/m^3$
N	7.132	$-$
$\mu_{sat,l}$	1.002×10^{-3}	$Pa \cdot s$
$\mu_{sat,v}$	9.727×10^{-6}	$Pa \cdot s$

TABLE 1: Saturation properties of water at $T_{ref} = 293.15K$.

17 is derived based on the isentropic relation $c = \sqrt{\frac{\partial p}{\partial \rho}}$ from the equation of state.

In the liquid-vapor mixture, a constant speed of sound of 1483.3 m/s is used, which is the speed of sound at saturation liquid density $\rho_{sat,l} = 998.1618\, kg/m^3$ at $T_{ref} = 293.15K$.

$$c = \begin{cases} \sqrt{(p_{sat} + B)\; N\; \frac{(\rho)^{N-1}}{(\rho_{sat,l})^N}} & , \text{ if } \alpha = 0 \\ 1483.3 m/s & , \text{ if } 0 < \alpha < 1 \end{cases} \tag{17}$$

The fluid density decreases sharply below the saturation pressure $p_{sat} = 2340\, Pa$ (which corresponds to $\rho_{sat,l} = 998.1618\, kg/m^3$) as seen in fig. 3 In this two-phase liquid vapor region, the speed of sound decreases significantly from 1483.3 m/s to below 10^{-1} m/s, plotted as "Barotropic two phase" in fig. 3, resulting in a discontinuity in the speed of sound c at the interface. As soon as cavitation appears,

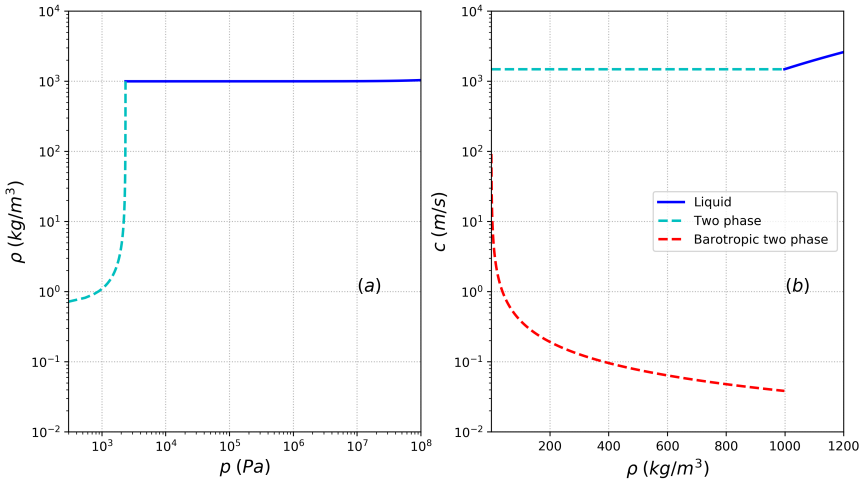

FIGURE 3: (a) Density vs pressure, (b) speed of sound vs density in the cavitation model.

such drastic decrease in c would make the flow supersonic locally resulting in spurious numerical oscillations. In the course of this work, we are interested in the generation and propagation of shock waves in the liquid phase and its interaction with solid wall. Therefore the speed of sound c is kept constant in the liquid-vapor mixture with the assumption that shock propagation in the cavitating region inside the bubbles is not of primary importance, whereas the shock propagation in the pure liquid phase is resolved accurately. To account for fluid viscosity μ, the liquid water phase is modelled with a constant viscosity $\mu_{sat,l}$. The dynamic viscosity in the liquid-vapor mixture is modelled with a quadratic law, following the model proposed in Beattie and Whalley (1982) in eq. 18 where the dynamic viscosity varies with the vapor volume fraction α.

$$\mu = (1 - \alpha)\left(1 + \frac{5}{2}\alpha\right)\mu_{sat,l} + \alpha\, \mu_{sat,v}, \text{ if } 0 < \alpha < 1 \tag{18}$$

The solver algorithm, temporal discretization and solution filtering has been validated on shock tube test case with an ideal gas as well as Rayleigh solution for 2D and 3D vapor bubble collapse detailed elaborately in Sarkar (2019).

2.3. Solid mechanics solver

The response of the solid is modelled with Cast3M which is a partial differential equations solver with the finite element method. In cavitation erosion, on one hand, the pressure loading varies over time and on the other hand, the importance of the forces of inertia has to be considered. The deterministic implicit solver is used to solve the non-linear solid mechanics equations to predict the response of solids to cavitation loads. It is worth mentioning that non linearities in solid can arise from different phenomenon such as non linearity of the material, like plasticity in metallic materials, shocks and impacts at structural interfaces or fluid-elastic forces from FSI. The deformation of solid within the elastic limit can be defined by Hooke's law in eq. 19 where $\underline{\underline{\sigma}}$ and $\underline{\underline{\varepsilon}}$ are the second order stress and strain tensor, $\underline{\underline{\underline{\underline{C}}}}$ is the 4^{th} order stiffness tensor. The total strain $\underline{\underline{\varepsilon}}$ can be decomposed into elastic and plastic strain components $\underline{\underline{\varepsilon}}_e$ and $\underline{\underline{\varepsilon}}_p$ respectively as in eq. 20.

$$\underline{\underline{\sigma}} = \underline{\underline{\underline{\underline{C}}}} : \underline{\underline{\varepsilon}}_e = \underline{\underline{\underline{\underline{C}}}} : (\underline{\underline{\varepsilon}} - \underline{\underline{\varepsilon}}_p) \tag{19}$$

$$\underline{\underline{\varepsilon}} = \underline{\underline{\varepsilon}}_e + \underline{\underline{\varepsilon}}_p \tag{20}$$

For a solid domain Ω, the equilibrium equation can be written as eq. 21, where $\underline{F}$ is the equivalent nodal force vector. The weak form of equilibrium equation after domain integration can be written as eq. 22 where $\underline{\underline{B}}$ is the discretized gradient operator.

$$\nabla \cdot \underline{\underline{\sigma}} = \underline{F} \tag{21}$$

$$\int \underline{\underline{B}}^T \underline{\underline{\sigma}} dV = \underline{F} \tag{22}$$

Assuming small deformations, the second order strain tensor can be further written as eq. 23, where $\underline{u_d}$ is the displacement vector :

$$\underline{\underline{\varepsilon}} = \frac{1}{2}(\nabla \underline{u_d} + \nabla (\underline{u_d})^T) \tag{23}$$

The finite element system transforms into eq. 24 after introducing the inertial and viscous effects where $\underline{\dot{U}}$ and $\underline{\ddot{U}}$ are the nodal velocity and acceleration vectors, $\underline{\underline{M}}$ is the mass matrix and $\underline{\underline{D}}$ is the damping matrix.

$$\underline{M} \cdot \underline{\ddot{U}} + \underline{\underline{D}} \cdot \underline{\dot{U}} + \int \underline{\underline{B}}^T \underline{\underline{\sigma}} = \underline{F} \tag{24}$$

The implicit time algorithm used for mechanical calculations is based on minimization of residuals at each mechanical step. At the beginning of each time step,

a residual imbalance is computed between the external applied forces $\underline{F}^{ext}$ and internal forces $\underline{F}^{int} = \underline{\underline{B}}^T \underline{\underline{\sigma}}$, representing the current state of the solid. The difference between these two forces at each node is the residual $R_i = \underline{F}^{ext} - \underline{F}_i^{int}$. The estimation of displacement at the next time step begins from this residual $\Delta U_{i+1} = \underline{\underline{K_e}}^{-1} R_i$, where $\underline{\underline{K_e}}$ is the elastic stiffness matrix at the beginning of the step. The new stresses $\underline{\underline{\sigma}}_{i+1}$ and strains $\underline{\underline{\varepsilon}}_{i+1}$ are calculated, giving the updated internal state of the solid $\underline{F}_{i+1}^{int}$. The new residual is estimated as $R_{i+1} = \underline{F}^{ext} - \underline{F}_{i+1}^{int}$. The procedure then uses a convergence loop to determine the increment of solution that minimizes the residual to the convergence criterion i.e. if $\|R_{i+1}\| \leq 10^{-4}$. The iteration ends if convergence is reached, else the step is repeated with incremental displacement until convergence is reached. Here we have introduced the basic steps for solid mechanics calculations for the understanding of our modelling approach. Additional details on the general formulation and solver methodology can be found in Di Paola et al. (2017a).

In our 2D computation, we assume a state of plane strain for the solid. The plane strain assumption imposes a strain state at a material particle such that non-zero strain components act only in one plane. The x-y plane is the one in which the strains are non-zero and the dimension of the solid in the z-direction is much larger than in the x and y directions. The fully three dimensional strain matrix reduces to a two dimensional one as a result since $\varepsilon_{xz} = \varepsilon_{yz} = \varepsilon_{zz} = 0$.

$$\begin{pmatrix} \varepsilon_{xx} & \varepsilon_{xy} & \varepsilon_{xz} \\ \varepsilon_{yx} & \varepsilon_{yy} & \varepsilon_{yz} \\ \varepsilon_{zx} & \varepsilon_{zy} & \varepsilon_{zz} \end{pmatrix} \Rightarrow \begin{pmatrix} \varepsilon_{xx} & \varepsilon_{xy} \\ \varepsilon_{yx} & \varepsilon_{yy} \end{pmatrix} \tag{25}$$

In this paper, three metal alloys aluminum alloy (Al-7075), duplex stainless steel (St A-2205) and nickel-aluminum-bronze (NAB) are considered. The materials are assumed to be homogenous, isotropic and thermal effects are neglected. The material constitutive law expressed in eq. (26) is used where an isotropic elastic-plastic solid deforms according to linear elastic equation when loaded below the yield strength σ_y, but deforms plastically if yield is exceeded. The plastic deformation is governed by the von Mises yield criterion with an isotropic hardening law known as *Ludwik equation*. The equation expresses the strain hardening as a function of plastic strain ε_p only. The constants K is the strength coefficient, n is the strain hardening exponent, E is the Young's modulus and the total strain can be decomposed into elastic strain ε_e and accumulated equivalent plastic strain ε_p.

$$\sigma_{VM} = \begin{cases} E\varepsilon_e & \text{, if } \sigma_{VM} < \sigma_y \\ \sigma_y + K\varepsilon_p^n & \text{, if } \sigma_{VM} > \sigma_y \end{cases} \tag{26}$$

The yield strength and material properties obtained with compression tests at a strain rate of $1.0\, s^{-1}$ are taken from Roy et al. (2015) and presented in table 2.

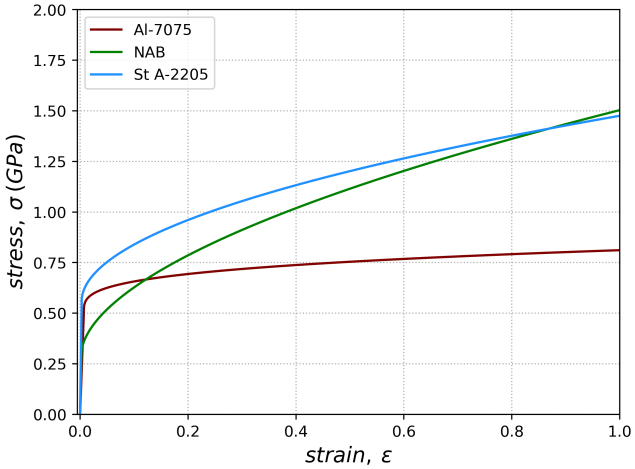

FIGURE 4: Stress-strain compression curves for Al-7075, St A-2205 and NAB at strain rate $1.0\ s^{-1}$.

The material behavior for Al-7075, St A-2205 and NAB depicting a typical elastic plastic response under compression tests is shown in fig. 4.

Material	$\sigma_y\ [MPa]$	$\rho\ [kg/m^3]$	$E\ [GPa]$	ν	$K\ [MPa]$	n
Al-7075	500	2810	71.9	0.33	312	0.29
St A-2205	560	7805	186	0.30	917	0.51
NAB	300	7580	122	0.32	1205	0.56

TABLE 2: Yield strength, material density, Young's modulus, Poisson's ratio and compressive properties at strain rate $1.0\ s^{-1}$ (Roy et al. (2015)).

An important parameter that will be used in our discussion is the von Mises stress σ_{VM} written in eq. (27) :

$$\sigma_{VM} = \sqrt{\frac{1}{2}[(\sigma_{xx} - \sigma_{yy})^2 + (\sigma_{yy} - \sigma_{zz})^2 + (\sigma_{zz} - \sigma_{xx})^2 + 6({\sigma_{xy}}^2 + {\sigma_{xz}}^2 + {\sigma_{yz}}^2)]} \tag{27}$$

It is used to determine whether an isotropic and ductile metal will yield when subjected to a complex loading conditions. The von Mises stress σ_{VM} is a scalar computed from the stress tensor and can be compared with the yield strength σ_y of the material which is another scalar. A material is said to starting to yield when $\sigma_{VM} \geq \sigma_y$.

Another important parameter is the accumulated plastic strain P_{ε_p} which characterizes the changes in the mechanical characteristics of material during the deformation hardening. It can be defined as the measure of the length of the flow

trajectory in the plastic strain space written as eq. (28).

$$P_{\varepsilon_p}(t) = \int_0^t \dot{P}(\tau) d\tau$$
$$\dot{P} = \sqrt{\frac{2}{3}\dot{\bar{\bar{\varepsilon}}}_p : \dot{\bar{\bar{\varepsilon}}}_p} = \sqrt{\frac{2}{3}\dot{\varepsilon}_p^{ij}\dot{\varepsilon}_p^{ij}} \tag{28}$$

3. Fluid-structure interaction

3.1. One-way coupling

In one-way fluid-structure coupling, we focus on the material response to hydrodynamic loads during cavitation bubble collapse. Such an approach is satisfactory if the solid wall displacement is sufficiently small. The behaviour of the solid wall can then be assumed to be almost rigid and no significant attenuation of hydrodynamic loads are expected. The staggered approach for one-way coupling treats the fluid and solid domains separately with independent numerical solvers - YALES2 for CFD and Cast3M for CSM. The fluid simulation of the bubble collapse is performed first, denoted as *CFD step 1*, where the boundary between the fluid and solid domain is treated as a rigid wall. Therefore $\underline{\dot{x}} = 0$ is used in eq. 2 & 3 to recover the Eulerian form of *Navier-Stokes* equations. In this purely CFD solution from initial time t_{in} to final simulation time t_{fin}, the pressure distribution $p(x,t)$ on the solid boundary is extracted at every coupling time Δt_{FSI} (constant in our case). After concluding the *CFD step 1*, the extracted space- and time-dependent pressure distribution $p(x,t)$ is applied to the solid as a time-dependent boundary condition (with a sampling time equal to Δt_{FSI}), in order to perform a purely solid mechanics simulation, denoted as *CSM step 1*. At the end of t_{fin}, the final state of solid response to the applied cavitation load is obtained in terms of resulting stress, interface displacement and accumulated plastic strain.

However, it is obvious that this procedure introduces some approximations as the feedback of the solid displacement on the fluid pressure, that is expected to relax partially, is totally neglected. The fluid domain does not deform to match the deformed solid boundaries at the fluid-structure interaction (FSI) interface, as seen in fig. 5. Therefore, with these assumptions, no coupling effects are introduced into the fluid domain.

3.2. Two-way coupling

To introduce the fluid-structure coupling effects in the fluid domain, a two-way coupled analysis is required where the solid wall displacement affects the subsequent fluid dynamics. In our analysis, we implement a *step-wise coupled approach* between the CFD and CSM domains which is an intermediate approach between uncoupled and strongly coupled FSI approach. Our *step-wise coupled approach* is based on an iterative procedure consisting in running several times

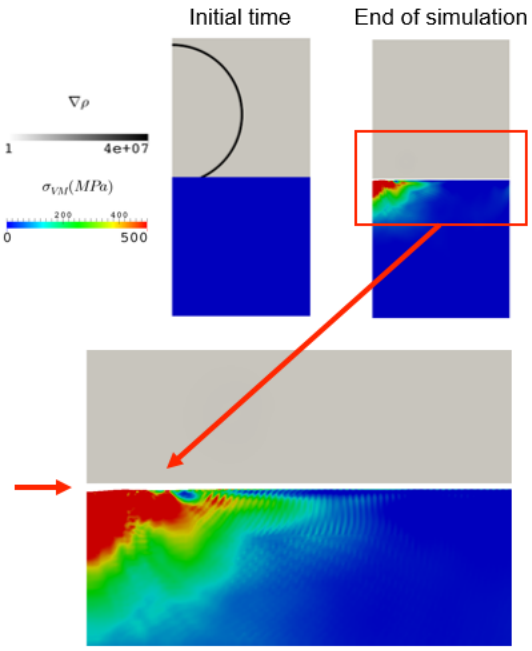

FIGURE 5: Non-matching fluid-solid domain boundaries after one-way FSI.

the full temporal evolution for both the fluid and the solid solvers. *CFD step 1* provides the initial estimates of pressure loads from t_{in} to t_{fin} at every Δt_{FSI} by assuming a rigid solid boundary, which is then used to compute the solid wall deformation in *CSM step 1*. Next, the time-dependent solid wall displacement at every Δt_{FSI} is introduced into a new fluid simulation from t_{in} to t_{fin}, denoted by *CFD step 2*. This step introduces a two-way coupling, but computed with a solid displacement that is overestimated since determined through the pressure load of *CFD step 1*, that is exerted on a non-compliant boundary. So, the pressure loads determined after introducing the FSI coupling effects are introduced into the *CSM step 2*. This step-wise iterative loop is repeated until convergence of pressure p and solid wall displacement u_d is established between successive CFD and CSM step shown in fig. 6. This means new CFD and CSM computations are carried out with newly predicted time-dependent boundary conditions up to a certain number of steps, and checked for convergence on (p, u_d) between the latest and the previous time steps. The advantage of this method is its simplicity since it does not require any communication between the fluid and the solid code during runtime. The obvious drawback is the need of performing multiple runs of simulation.

A coupling has to be implemented between the fluid and solid domain by means of dynamic and kinematic interface conditions. The pressure and shear load from the fluid side has to be in equilibrium with the traction at the boundary of the solid at the fluid-solid interface (dynamic interface condition). Since the order of magnitude of shear loads (based on estimations from literature) are much smaller

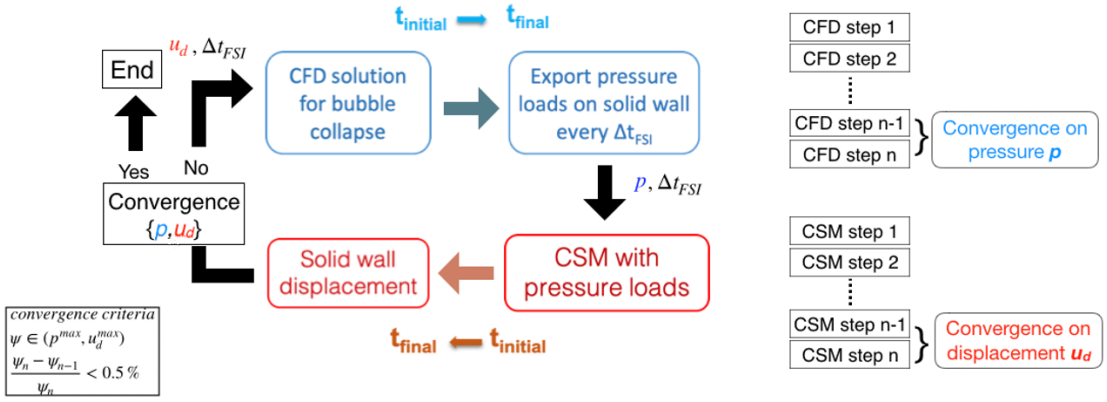

FIGURE 6: Step-wise two-way fluid-structure interaction procedure.

in comparison to the normal pressure loads in our simulations, we neglect the shear loads at the interface boundary.

In addition, the normal velocity of the solid must equal the fluid velocity at the fluid-solid interface (kinematic interface condition). This is achieved by solving the ALE form of the *Navier-Stokes* equations in the fluid solver. In order to define a fluid mesh movement able to describe the domain deformation, but limiting the deformation of single mesh elements, the displacement at the fluid-solid interface is distributed on the position of the nodes of the ALE mesh in the rest of the fluid computational domain. In order to achieve a uniform ALE mesh element deformation, the fluid interface velocity is imposed to match the velocity of the solid interface determined by the solid solver. At the opposite end of the fluid computational domain, the boundary displacement is kept equal to zero. The node velocity anywhere else in the domain is evaluated by linear interpolation based on the node position between both ends of the computational domain.

4. One-way vs two-way coupling

In this paper, we have pursued the case of shock-induced bubble collapse attached to the solid wall. The attached bubble is initially at a stand-off distance $\gamma = 0.9$ with an initial bubble radius $R_0 = 495\mu m$. Stand-off distance $\gamma = h/R_{max}$ is the non-dimensional distance of the bubble from the solid wall, where h is the distance between the solid wall and bubble center at the time of formation, R_{max} is the maximum bubble radius. The two-way FSI for a detached bubble collapse ($\gamma > 1$) has not been pursued in this paper. Indeed based on our study of one-way FSI for detached bubble collapse at stand-off distance $\gamma > 1$ (Sarkar (2019)), we anticipate the effect of two-way FSI on detached bubble case to be very small. A detached bubble collapse is predominantly the emission of a shock wave at a distance from the wall during collapse and the response of material to the shock wave propagation on the wall. There will be practically no effect of solid wall de-

formation on the resulting bubble dynamics as the bubble collapses far from the wall. The interaction of the shock with the solid wall is marked with very small plastic strain and surface displacement at an offset from the bubble center.

The initial condition for the fluid simulation is a 2D vapor bubble surrounded by water at atmospheric condition. Both the fluids are at rest at time $t = 0\,s$ and a shock front at a distance of $2\,mm$ from the solid wall is initiated to drive the shock-induced collapse.

$$\begin{aligned} &liquid: \ \rho_l = 998.2\,kg/m^3, \ p = 101,325\,Pa, \\ &vapor: \ \rho_v = 10\,kg/m^3, \ p = 2194\,Pa. \end{aligned} \tag{29}$$

The vapor bubble is initialized with a hyperbolic tangent function given in eq. 30 assuming a continuous density profile through the phase interface. Here ρ_v is the liquid-vapor mixture density corresponding to p_v^{sat} and ρ_l is the pure liquid density. The pressure in the domain is initialized from ρ_v and ρ_l using the equations of state. In eq. 30, Δx is the computational mesh spacing, x_i is the spatial coordinate, x_c is the position of the bubble center and d_f is the analytical distance function to the interface, defined in eq. (31).

$$\rho_{init} = \rho_v + \left(\frac{\rho_l}{2} + \frac{\rho_l}{2} \times \tanh\left(\frac{d_f}{\Delta x} \right) \right) \tag{30}$$

$$d_f = \sqrt{\sum_{i=1}^{ndim} (x_i - x_c)^2} \ - \ R_0 \tag{31}$$

The initial bubble radius is $R_0 = 500\,\mu m$ and the fluid computational domain size is taken as $10R_0 \times 5R_0$ shown in fig. 7, with around $500,000$ computational cells. A region of $1 \times 1\ mm^2$ is meshed with uniformly spaced structured quadrilateral cells ($\Delta x = \Delta y = 5\mu m$), in which the bubble is initialized. The rest of the domain is meshed with unstructured quadrilateral cells with a growth ratio of 1.05 towards the domain boundary. Only one half of 2D bubble collapse is simulated taking advantage of the symmetry. The outlet fluid boundaries at $10R_0$ in the positive x-direction and at $5R_0$ in the y-direction are treated with Navier-Stokes Characteristic Boundary Conditions (NSCBC) following Poinsot and Lele (1992). The NSCBC boundaries are modelled to treat propagation of shock waves only in the boundary normal direction and to be weakly reflective. The solid wall is at the bottom of the fluid computational domain, which serves as the FSI interface between fluid and solid. The solid computational domain is taken as $2R_0 \times 5R_0$. Only $1\ mm$ of the FSI coupling interface is considered as most of the dynamic forces act on this length, therefore reducing the solid domain considerably in the positive x-direction. This is made possible due to the use of wave absorbers in the solid external boundaries and has been extensively tested to validate that the dynamics in the solid domain is independent of the boundary position. The solid

computational domain is meshed with multiple layers of quadrilateral elements and few triangular element layers with 9850 finite elements and 29065 nodes.

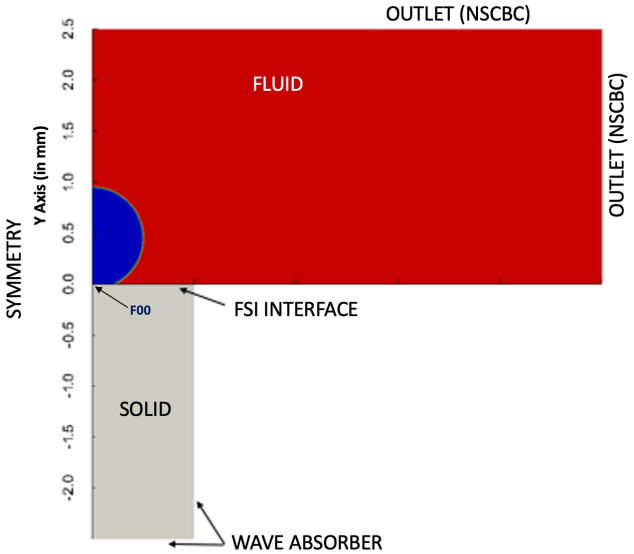

FIGURE 7: FSI coupling domain and interface between the fluid and solid, bubble radius $R_0 = 500\,\mu m$, (*bottom*) solid domain, size $= 1 \times 2.5\,mm^2$, (*top*) fluid domain, size $= 5 \times 2.5\,mm^2$.

The initial bubble radius is resolved with 100 computational cells. A limiting $CFL = 0.01$ and $CFL_{acou} = 0.5$ is used in the simulation to ensure stability of the time advancement scheme. As discussed, in our cavitation model there is a sharp decrease of fluid density at the interface and large time steps could give rise to numerical instability. In our entire fluid simulation of total simulation time $t_{fin} = 6\,\mu s$, the computational time step stays lower than $1\,ns$ and the smallest time step Δt is recorded to be $0.05\,ns$ occurring during the most dynamical part of the simulation. We employ a solution filtering of the density field at every 40 iterations, and filtering of the pressure field at every iteration. An artificial viscosity constant $C_\mu = 0.1$ and artificial viscosity order $r = 4$ is used, implying a 4^{th} order artificial viscosity model.

The fluid domain boundary at the fluid-solid interface, of $1mm$ length, is resolved with 201 computational nodes with uniform grid spacing where the time-dependent pressure evolution is extracted at every Δt_{FSI}. The solid domain boundary is resolved with 801 nodes with a uniform grid spacing at the fluid-solid interface, where the time-dependent pressure loading is applied. The number of computational nodes in both fluid and solid interfaces is verified with grid independence study. The solid interface needs more computational nodes to accurately resolve the plasticity generated from the moving shock waves with varying shock speed across the interface. Consequently, the pressure from the fluid nodes is interpolated using a quadratic function and distributed to the 801 nodes on the

solid domain boundary at the fluid-solid interface. The time and space-dependent pressure is applied as a time-dependent boundary condition every Δt_{FSI} on the interface in the solid simulation *CSM step 1*. In one-way FSI, the coupling time step is $\Delta t_{FSI} = 5\ ns$ and time-step independence studies up to $\Delta t_{FSI} = 1\ ns$ showed no difference in the results.

4.1. One-way FSI

A planar shock front of 50 MPa is initiated at $t = 0s$ at a distance of $2mm$ from the solid wall. The shock front hits the bubble upper surface at $t = 0.68\ \mu s$ and the solid wall at $t = 1.3\ \mu s$. The shock front is promptly reflected back from the solid wall, as it can be seen in the temporal evolution of bubble collapse presented in fig. 8. In each frame of the figure, the left contour is the density field and the right contour is the pressure field. The events of bubble collapse up to $t = 4\ \mu s$ is the shrinking of bubble volume and initial stages of liquid jet formation, piercing through the bubble upper surface moving towards the wall. It is interesting to note that untill $t = 4\ \mu s$, the only pressure loading on the wall is the initial shock front impact. The liquid jet impacts the wall at $t = 4.294\ \mu s$ with an impact pressure

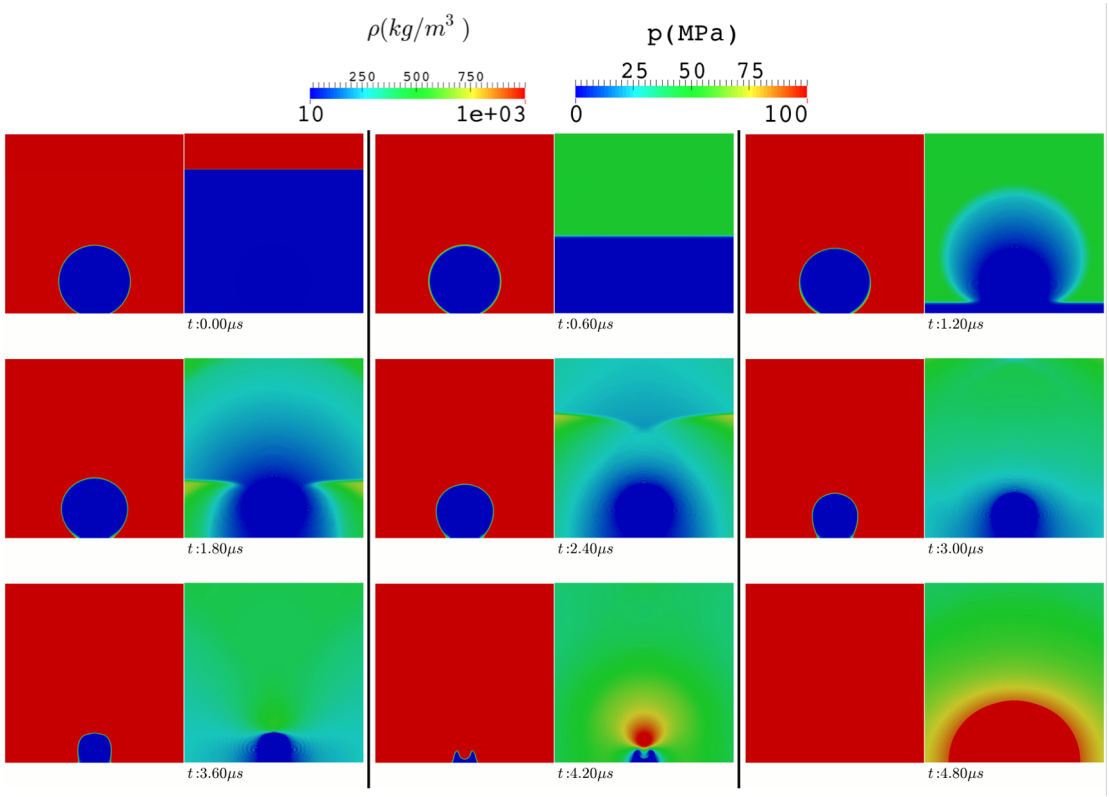

FIGURE 8: Temporal evolution of a shock induced 2D attached bubble collapse : $(left)$ density and $(right)$ pressure contour , $\gamma = 0.9$, $R_0 = 495\ \mu m$, $p = 0.1\ MPa$, $p_{shock} = 50\ MPa$, frame size $= 4 \times 2.5\ mm^2$.

of 1.97 GPa. This is the water hammer pressure exerted by the liquid jet on the wall. This dynamical part of bubble collapse is explained with the aid of fig. 9 & 10. There are two curves in fig. 9 representing pressure p_{F00} and $p_{max-wall}$. The curve p_{F00} is the pressure on the wall at the bubble axis of symmetry (pt. F00) and $p_{max-wall}$ is the instantaneous maximum pressure on wall. The same peak of curve p_{F00} and $p_{max-wall}$ indicates that the pressure peak is at pt. F00 located at bubble axis of symmetry. The position of pressure $p_{max-wall}$ can be determined from the recorded data of maximum pressure and its position. The liquid jet after

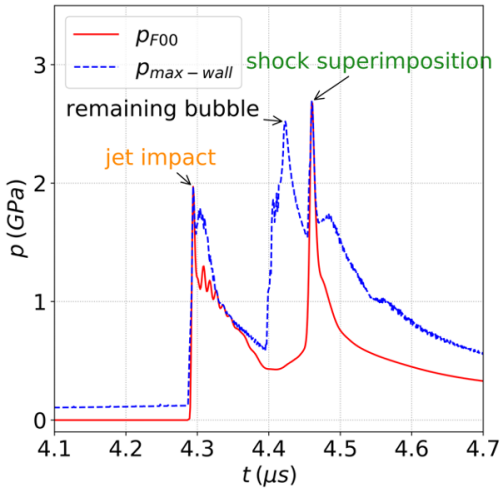

FIGURE 9: Temporal evolution of pressure p_{F00} at point $F00$ and maximum pressure on wall $p_{max-wall}$, $\gamma = 0.9$, $R_0 = 495\,\mu m$, $p = 0.1\,MPa$, $p_{shock} = 50\,MPa$.

impacting the wall moves away from the bubble axis of symmetry with a velocity of over $500\,m/s$ shrinking the remaining bubble volume. The remaining bubble volume in 2D is the equivalent of 3D torus after the liquid jet pierces the bubble volume. This flow induced collapse of the remaining bubble volume produces the second pressure peak of 2.52 GPa at $t = 4.423\,\mu s$. The second pressure peak is not at the bubble axis of symmetry, but located at an offset of $0.1\,mm$ from pt. $F00$. The remaining bubble collapse emits shock waves which travel along the wall towards the bubble axis of symmetry. The superimposition of shock waves leads to the strong compression of liquid near pt. $F00$ giving rise to the third pressure peak of 2.69 GPa at $t = 4.46\,\mu s$.

The evolution of von Mises stress σ_{VM} during the collapse is shown in fig. 10 for Al-7075 ($E = 71.9$ GPa; $\sigma_y = 500$ MPa). The scale for maximum σ_{VM} has been fixed at 500 MPa to show the regions exceeding the yield stress σ_y of the material. These are the regions where the material will yield under loading. At $t = 4.3\,\mu s$, the liquid jet impact on the wall is seen at pt. $F00$ with the impact load propagating in the solid as elastic waves. The resulting surface displacement in Al-7075 is $3.8\,\mu m$ at the bubble symmetry axis. Comparatively, the surface dis-

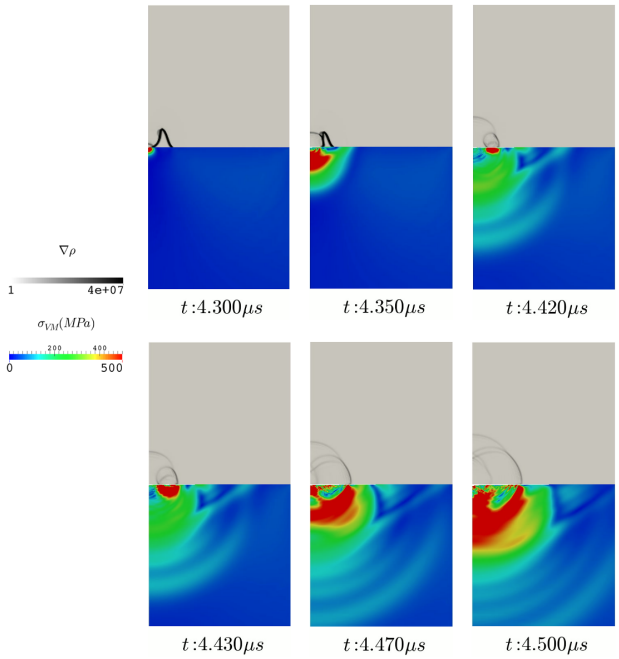

FIGURE 10: Evolution of von Mises stress in solid : (*top*) numerical schlieren of bubble collapse and (*bottom*) von Mises stress σ_{VM} on each frame, $\gamma = 0.9$, $R_0 = 495\,\mu m$, $p = 0.1\,MPa$, $p_{shock} = 50\,MPa$, frame size $= 1 \times 2\,mm^2$.

placement in NAB is 2.6 μm and St A-2205 is 1.4 μm. The surface displacement after the liquid jet impact at pt. $F00$ is plotted in fig. 11. Next is the collapse of the remaining bubble at an offset of 0.1 mm from pt. $F00$ seen at $t = 4.420$ in fig. 10. The resulting surface displacement from the remaining bubble collapse is seen on the final wall interface profile presented later. The emitted shock from the remaining bubble collapse travels along the wall towards the bubble axis of symmetry seen at $t = 4.43\,\mu s$. The superimposition of the shock waves near pt. $F00$ seen at $t = 4.47\,\mu s$ gives another pressure loading at the bubble axis of symmetry. This leads to further surface displacement with the shock and elastic wave subsequently propagating and attenuating in their respective domains. The maximum plastic deformation at the end of simulation i.e. $t = 6\,\mu s$ is observed for NAB of 5.1 μm at the bubble axis of symmetry. The yield strength of NAB is 300 MPa which is the least of all the three materials considered. In comparison, the maximum plastic deformation in Al-7075 is 4.6 μm and in St A-2205 is 1.6 mum. The temporal evolution of surface displacement at pt. $F00$ is plotted in fig. 11(a) which shows the displacement after liquid jet impact and shock superimposition. The temporal convergence of the final surface displacement is verified by running the solid simulation for an extended time $t_{fin} = 11\,\mu s$ shown in 11(b). Finally the results of one way FSI coupling is summarized in table 3 with the values of the maximum accumulated plastic strain $P^{max}_{\varepsilon_p}$ and the area under plastic deforma-

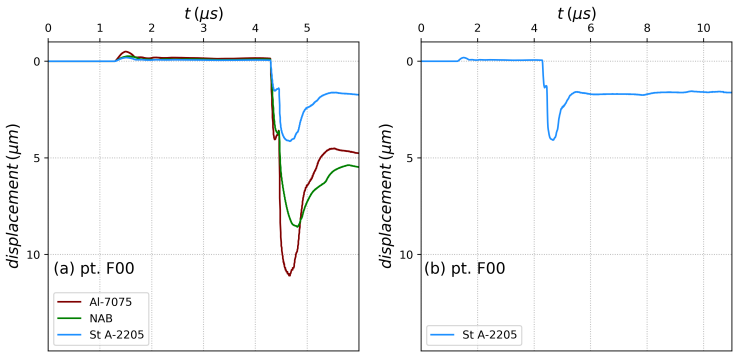

FIGURE 11: Temporal evolution of surface displacement at point $F00$, (left) until $t = 6\mu s$, (right) until $t = 11\ \mu s$.

tion A_{ε_p}. The plasticity developed in the solid is quantified with A_{ε_p} representing surface area undergoing a minimum of 0.5% plastic strain. The discussion on $P^{max}_{\varepsilon_p}$ contours and final interface profile from one-way coupling is discussed with the two-way coupling results.

Material	$P^{max}_{\varepsilon_p}$	$A_{\varepsilon_p}\ (m^2)$
Al-7075	0.255	5.523×10^{-8}
NAB	0.0972	9.816×10^{-8}
St A-2205	0.0856	2.052×10^{-8}

TABLE 3: Maximum accumulated plastic strain $P^{max}_{\varepsilon_p}$ and area under plastic deformation A_{ε_p} for shock induced attached bubble, $\gamma = 0.9$, $R_0 = 495\ \mu m$, at $t = 6\ \mu s$.

4.2. Two-way FSI

In two-way coupling, the resulting boundary displacement on the 801 nodes on solid interface from *CSM step 1* is extracted at every Δt_{FSI} and interpolated using cubic spline interpolation to the 201 fluid nodes to perform *CFD step 2*. In our case setup, we use a uniform grid spacing in both the fluid and solid interface, resulting in matching between all of the fluid nodes and some of the solid nodes, as long as the fluid-structure interface is not deformed. In the case of fluid-structure interface displacement, the solid nodes could possibly move both in x & y direction under the influence of normal stresses, so that the matching between all of the fluid nodes and some of the solid nodes cannot be verified at all stages of the simulation. Therefore cubic spline interpolation is used to transfer the surface displacement irrespective of grid resolution in the two-way FSI procedure. This procedure allows an accurate representation of the interface displacement even in the case of arbitrary (i.e. non uniform and/or non-matching) meshing for the coupling interface.

A second step of an entirely new fluid simulation is performed using the time-dependent boundary displacement on 201 fluid nodes introduced every Δt_{FSI}. The nodal pressures on the fluid interface from this second fluid simulation is extracted every Δt_{FSI} and introduced into the solid simulation exactly as the first step. It is followed by the second solid simulation and the boundary displacement is extracted to be introduced on the subsequent fluid step.

These step-wise fluid and solid simulations are performed separately until convergence of pressure and boundary displacement is reached between successive steps. In our analysis, four steps of fluid and solid simulations are performed with pressure and displacement exchanged at $\Delta t_{FSI} = 1\ ns$. The solution convergence is defined by the relative difference below 0.5% in both the maximum pressure for CFD and the maximum displacement for CSM between two successive steps. For example in the case of St A-2205 out of the total decrease in the water hammer pressure Δp_{wh} during liquid jet impact, there is a relative decrease of 81% of Δp_{wh} in the second fluid step and about 19% in the third fluid step of the simulations. The relative difference between the third fluid step and fourth fluid step is 0.3% at which point a convergence of the numerical prediction is considered as achieved. The damping of pressure and convergence of wall pressure $p_{max-wall}$ after four steps in our FSI analysis for St A-2205 is shown in fig. 12. The time step used in the solid solver is bigger than the one needed by the fluid solver.

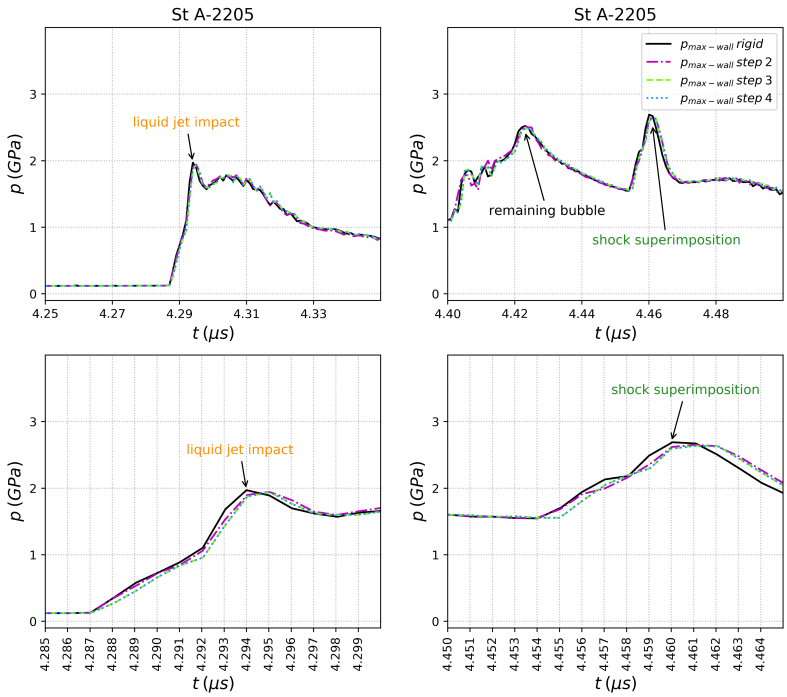

FIGURE 12: Pressure damping in *step-wise coupled* FSI showing convergence of pressure on St A-2205 in four steps - shock induced attached bubble collapse $\gamma = 0.9$, $R_0 = 495\ \mu m$.

Despite the apparent simplicity of the proposed step-wise two-way coupling approach, care needs to be taken in the choice of the coupling time step w.r.t. the time steps in the CFD and CSM solvers. Indeed, those two time-steps can be different, the CFD time step being typically smaller. In this case, a time interpolation of the solid wall displacement needs to be applied when this displacement is communicated to the CFD solver. This may cause an early response of the fluid to a solid deformation. In order to avoid this numerical artefact, we have reduced Δt_{FSI} to the value taken by the fluid solver, i.e. 1 ns.

4.3. Effect of solid deformation on fluid pressure

We start the analysis of the results by first comparing the maximum wall pressure $p_{max-wall}$ for shock-induced 2D bubble collapse plotted in fig. 13. The temporal evolution of pressure on the rigid wall and deformable wall of Al-7075, NAB are St A-2205 are plotted. To recall the pressure peaks on rigid wall, the first

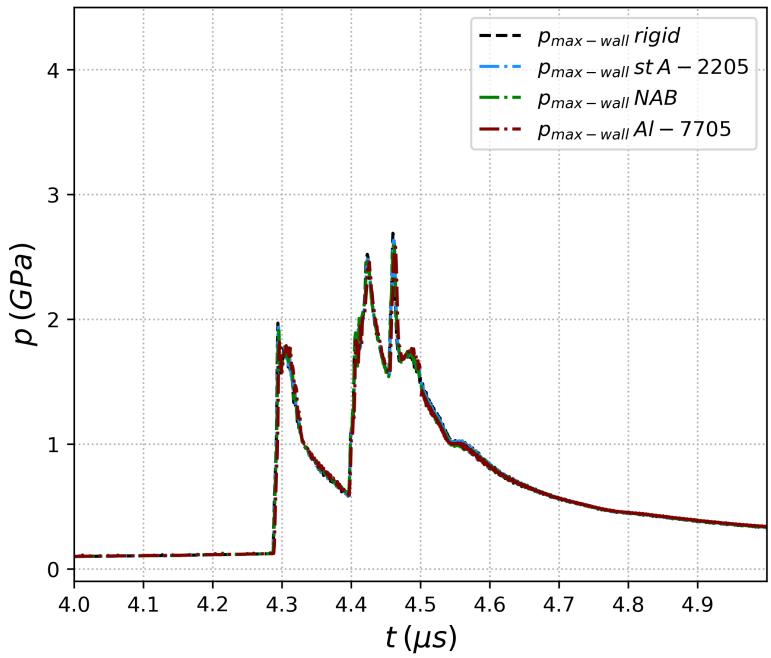

FIGURE 13: Maximum pressure $p_{max-wall}$ evolution on rigid wall and on the deformable materials with two-way FSI, shock-induced attached bubble collapse $\gamma = 0.9$, $R_0 = 495\,\mu m$.

peak of $1.97\,GPa$ at $4.294\,\mu s$ is the water hammer pressure p_{wh} from the liquid jet impact at the bubble symmetry axis. The second peak of $2.52\,GPa$ at $4.423\,\mu s$ is the remaining bubble collapse at an offset of $0.1\,mm$ from the bubble symmetry axis. This remaining bubble collapse emits shock waves. The superimposition of these shock waves with their symmetric images at the symmetry axis give rise to the third peak of $2.69\,GPa$ at $4.46\,\mu s$.

We will now investigate in detail the first pressure peak from the liquid jet impact shown in fig. 13 with the aid of the zoom plotted in fig. 14. The maximum

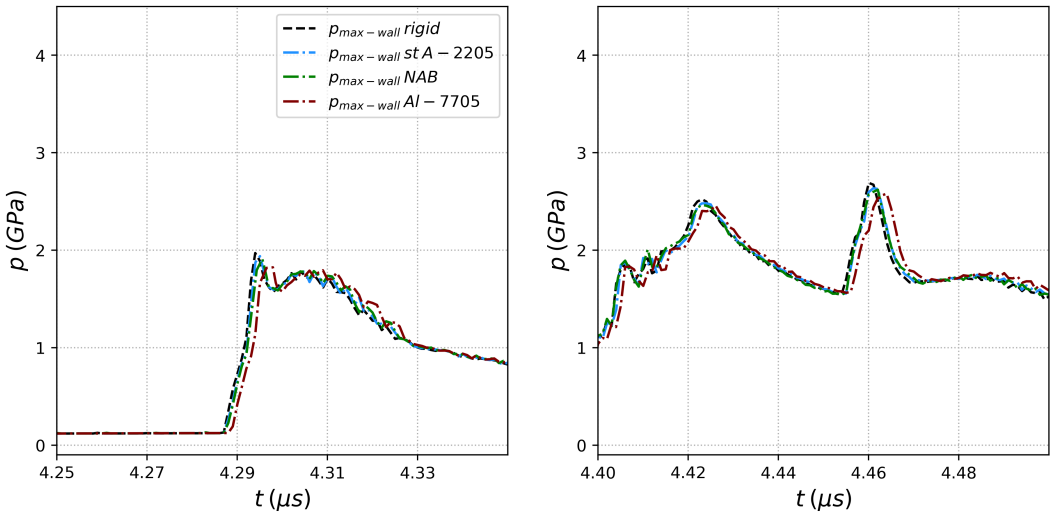

FIGURE 14: Zoomed-in on maximum pressure $p_{max-wall}$ evolution on rigid wall and on the deformable materials with two-way FSI, shock-induced attached bubble collapse $\gamma = 0.9$, $R_0 = 495\ \mu m$.

pressure recorded on a deformable Al-7075 wall at the bubble symmetry axis is $1.82\ GPa$ at $4.297\ \mu s$. Al-7075 is the softest of the three materials and has the lowest slope in the elastic regime of the $\underline{\underline{\sigma}} - \underline{\underline{\varepsilon}}$ curve. It is expected to provide the maximum damping to the pressure load out of the three materials. The first pressure peak for deformable NAB and St A-2205 wall are $1.91 GPa$ and $1.94 GPa$ respectively with time shift due to damping of $1.5\,ns$ and $1\,ns$. The pressure peak decreased about 8% in Al-7075 at the time of liquid jet impact in comparison to the rigid wall. Similarly the decrease in pressure peaks for NAB and St A-2205 are 3% and 1.5% respectively. We can compare the computed impact pressure of liquid jet for different materials with the theoretical expression of the dampened pressure for a one-dimensional system in eq. (32) which depends on the ratio of the liquid and the solid acoustic impedances ρc.

$$\Delta p = \frac{(\rho_l c_l u_l)}{1 + (\rho_l c_l / \rho_s c_s)} \tag{32}$$

Two shock waves are created on the impact of liquid jet - one shock propagating in the solid and one shock reflecting back into the liquid. The numerator $\rho_l c_l u_l$ is the water hammer pressure for the liquid jet of velocity u_l on a perfectly rigid wall, $\rho_l c_l$ is the acoustic impedance of the liquid and $\rho_s c_s$ is the acoustic impedance of the solid, which is related to the Young's modulus E by $\rho_s c_s = \sqrt{\rho_s E}$. The ratio

of acoustic impedances ($\rho_s c_s / \rho_l c_l$) is infinite for a perfectly rigid wall, whereas for a perfectly compliant wall it is zero.

The differences between the numerical results and theoretical estimations from eq. (32) for Al-7075, NAB and St-A2205 are about $2\%, 1.5\%$ & 2% as reported in table 4. In comparison, for three-dimensional simulations Chahine and Hsiao (2015) reported a total damping in pressure peaks of approximately 6% and 3% for Al-7075 and St A-2205 respectively. It is important to highlight that the 3D results were obtained for different initial conditions, i.e. bubble of $R_{max} = 2\,mm$ at $\gamma = 0.75$ collapsing at an ambient liquid pressure of $0.1\,MPa$ and therefore, are not directly comparable. The comparisons for the pressure damping has been summarized in table 4. For Al-7075 our simulation gives a damping of 8% for the pressure peak from liquid jet impact. The predicted damping lies in between the 1D and 3D results, indicating a role played by multidimensional flow dynamics on pressure damping effects. Whereas in the case of St-A2205, we obtain only a decent agreement with the 1D and 3D results. This in our opinion highlights the need for a much detailed study on the effects of multi-dimensional dynamics on pressure damping by surface displacement.

Material	Theoretical eq. (32)	Present study	Chahine and Hsiao (2015)
	1D	2D	3D
Al-7075	10%	8%	6%
NAB	4.5%	3%	-
St A-2205	3.5%	1.5%	3%

TABLE 4: Comparison of pressure damping between the present study, theoretical estimation and existing literature.

We can now proceed to the analysis of the second and third pressure peaks. From fig. 14, we find the behaviour of NAB and St-A2205 much closer to each other, and to the rigid wall case, in comparison to Al-7075. The predicted pressure peaks for the three different events generating pressure peaks on the wall, i.e. liquid jet impact, remaining bubble collapse and shock wave superimposition during bubble collapse for the rigid wall and the considered materials have been summarized in table 5. The pressure decrease due to damping in Al-7075 is about 2.7% in the second pressure peak from remaining bubble collapse and 4.5% in the third pressure peak from shock wave superimposition at the symmetry axis.

The numerical Schlieren and accumulated plastic strain P_{ε_p} contour for St A-2205 presented in fig. 15 show the different salient features of the two-way coupling simulation in the final FSI iteration step. Data is mirrored in both the fluid and solid domains along the Y-axis for visualization. At $t = 4.320 \mu s$ after the liquid jet impact on the wall, the first sign of plasticity near the bubble symmetry axis can be seen. The water hammer shock formed at the liquid jet impact on the wall can be seen moving back towards the liquid domain at $t = 4.320\,\mu s$ and $t = 4.365\,\mu s$.

	Peak 1	Peak 2	Peak 3
Material	Liquid jet	Remaining bubble collapse	Shock superimposition
	in GPa		
Rigid	1.97	2.52	2.69
Al-7075	1.82	2.45	2.57
NAB	1.91	2.46	2.62
St A-2205	1.94	2.48	2.63

TABLE 5: Comparison of estimated pressure loads at different dynamical events during bubble collapse for the rigid wall and the considered materials - attached bubble $\gamma = 0.9$, $R_0 = 495\,\mu m$.

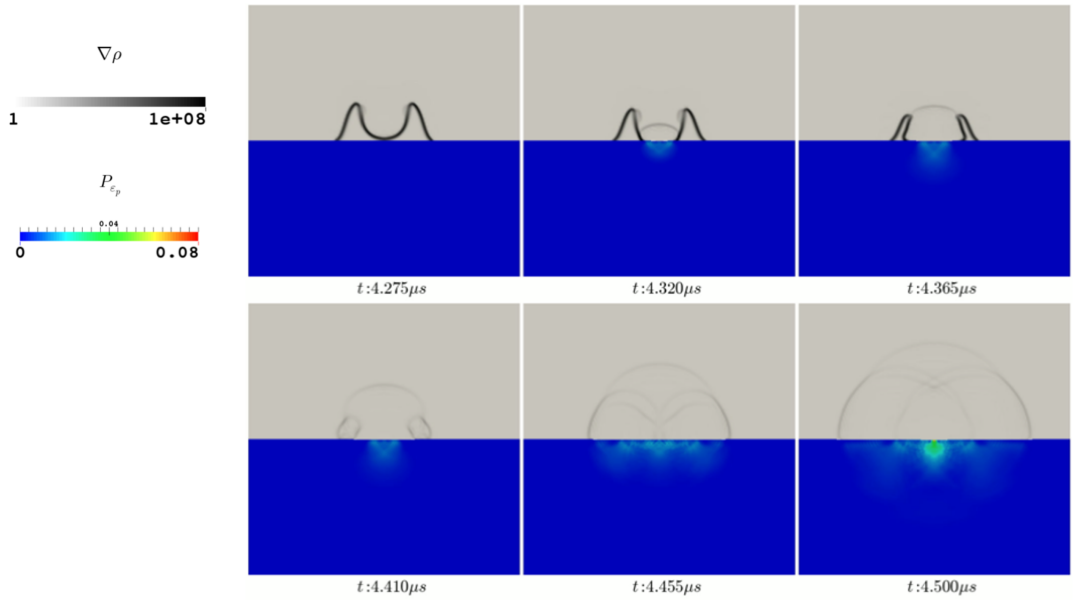

FIGURE 15: Numerical schlieren and accumulated plastic strain P_{ε_p} in two-way FSI for St A-2205 at different time instants showing the dynamical features of bubble collapse and corresponding generation of plasticity, shock-induced attached bubble collapse $\gamma = 0.9$, $R_0 = 495\ \mu m$, $p = 0.1\ MPa$, $p_{shock} = 50\ MPa$, frame size=$1 \times 1\ mm^2$.

This shock wave also propagates along the wall with the compressing inner surface of the remaining bubble and generates plasticity along the wall. The fluid interface movement matches the solid surface deformation in the simulation, thus giving a conforming fluid-solid physical domain with matching interface deformation. The relative error in the displacement of the fluid and solid interface is about 0.0023%. The next sequence is the collapse of remaining bubble at an offset of about $0.1mm$ from the symmetry axis, which is accompanied by the emission of another shock. This shock wave produced at an offset travels along the solid surface and later focuses on the symmetry axis. The generation of plasticity from the propagating shock waves can be seen at $t = 4.455\mu s$. Finally, the superimposition of the shocks at the symmetry axis triggers the final pit formation by generating additional plastic strain in the already plasticized area.

4.4. Effect on material response

A comparison of the maximum accumulated plastic strain $P_{\varepsilon_p}^{max}$ and surface area under plastic deformation A_{ε_p} can be drawn between the two-way and one-way computations. Figure 16 shows the contours for accumulated plastic strain P_{ε_p} in the materials obtained with one-way and two-way FSI.

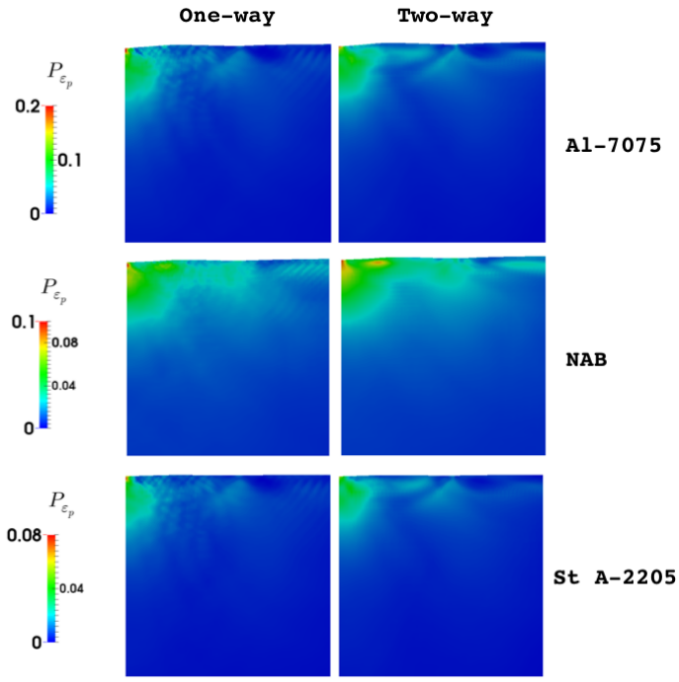

FIGURE 16: Comparison of accumulated plasticity P_{ε_p} contour for one-way and two-way coupled FSI at $t = 6\,\mu s$, shock-induced attached bubble collapse $\gamma = 0.9$, $R_0 = 495\,\mu m$, frame size=$250 \times 250\ \mu m^2$.

Table 6 lists the $P_{\varepsilon_p}^{max}$ and A_{ε_p} obtained from two-way coupled simulation for the materials Al-7075, NAB and St A-2205. It also lists the reduction in $P_{\varepsilon_p}^{max}$

and A_{ε_p} due to pressure relaxation from surface deformation in our two-way FSI, compared to one-way FSI. To recall for Al-7075, the decrease in peak pressures on the wall during the three dynamical events during attached bubble collapse is 8%, 2.7% and 4.5%, and its resulting effect on $P^{max}_{\varepsilon_p}$ and A_{ε_p} is summarized in table 6. The maximum accumulated plastic strain $P^{max}_{\varepsilon_p}$ decreases considerably for

Material	$P^{max}_{\varepsilon_p}$	$A_{\varepsilon_p}\,(m^2)$	reduction in $P^{max}_{\varepsilon_p}$	reduction in A_{ε_p}
Al-7075	0.191	5.3291×10^{-8}	25%	3.5%
NAB	0.101	9.2381×10^{-8}	-3%	6%
St A-2205	0.0608	2.0062×10^{-8}	30%	2.3%

TABLE 6: Maximum accumulated plastic strain $P^{max}_{\varepsilon_p}$, surface area under plastic deformation A_{ε_p}, reduction in $P^{max}_{\varepsilon_p}$ and A_{ε_p} in two-way vs one-way FSI at $t = 6\,\mu s$ for Al-7075, NAB and St A-2205, shock-induced attached bubble collapse $\gamma = 0.9$, $R_0 = 495\,\mu m$..

both Al-7075 and St-A2205 due to pressure relaxation in two-way FSI, whereas for NAB it does not change considerably between one-way and two-way FSI, in fact a slight increase is observed. This reveals NAB's sensitivity in developing plastic strain due to its low yield strength in comparison to the magnitudes of impacting pressure loads. Similar to what we have seen before, NAB produces the maximum plasticized area in comparison to Al-7075 and St-A2205. The decrease in plasticized surface area is also highest in NAB, again owing to its lower yield strength.

In our final analysis, we draw comparisons of interface shape for the three materials at the final simulation time of 6 μs presented in fig. 17. We find similar pit shapes in one-way and two-way simulation for the three materials in the case of shock-induced attached bubble collapse. The relative difference in the final interface position between one-way and two-way coupling is maximum in Al-7075 followed by NAB and St A-2205 respectively. This can be explained with material properties plotted in fig. 4. Although Al-7075 has higher yield strength σ_y than NAB ($500\,MPa$ in comparison to $300\,MPa$), the strain hardening exponent n for Al-7075 is lower in comparison to NAB (0.29 in comparison to 0.56). It implies that NAB would start to plasticize sooner and at lower impact loads due to its lower σ_y. On the other hand, comparatively lower impact load beyond the material yield strength will be needed to produce similar plastic strain in Al-7075 in comparison to NAB as evidenced from the plasticity curve of the stress-strain plot in fig. 4. This also explains the highest magnitude obtained for maximum accumulated plastic strain $P^{max}_{\varepsilon_p}$ for Al-7075 in comparison to other materials. The highest relative difference in the final interface position for Al-7075 highlights the material behaviour of maximum damping of the impact pressure loads. NAB, although allowing far less surface deformation and damping, responds with much larger plasticized surface area. The behaviour of St A-2205 is much similar to rigid wall, although it damps more the pressure peak generated by the shock waves

superimposition, about 2.3%, in comparison to 1.5% of pressure from liquid jet impact.

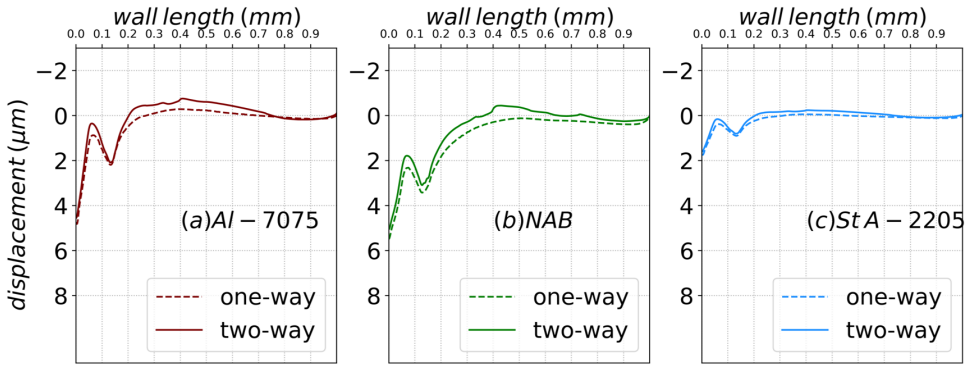

FIGURE 17: Comparison of solid interface profile for one-way and two-way coupled FSI, shock-induced attached bubble collapse $\gamma = 0.9$, $R_0 = 495\ \mu m$.

As we have highlighted throughout the course of this work, an attached bubble collapse is a complex dynamical event dominated by many interconnected physical features which determine the resultant pressures on the wall. There are multiple shock waves impacting and propagating on the solid wall, the magnitude of which are often many orders higher in comparison to detached bubble collapse. The decrease in maximum accumulated plastic strain$P_{\varepsilon_p}^{max}$ is considerable in two-way coupling for an attached bubble collapse, for example about 30% in St A-2205. On the other hand, the area under plastic deformation A_{ε_p} decreases by about 3.5%, 6%, 2.3% for Al-7075, NAB and St A-2205 respectively.

5. Conclusions

In this paper, we carried out a comparative study of material responses for aluminum alloy Al-7075, nickel-aluminum bronze alloy (NAB) and duplex stainless steel (St A-2205) with one-way and two-way coupling for a shock-induced collapse of a bubble initially attached to the wall. We investigated the effect of surface deformation on the resulting pressure peaks induced by a single bubble collapse with two-way coupled FSI. Two-way coupled fluid-structure interaction simulations show that the pressure load is damped on the material with surface deformation. The decrease in pressure loads are higher when the surface deformation is high due to increased pressure relaxation in the fluid. The pressure from liquid jet impact on Al-7075 decreases by 8% whereas the decrease of pressure peaks due to the remaining bubble collapse and to shock wave superimposition is 2.7% and 4.5% respectively. In comparison to one-way coupled prediction of material response, decrease in pressure peaks in two-way coupling resulted in decrease of 25% in the maximum accumulated plastic strain and 3.5% of total plasticized

area in Al-7075. On the other hand, the behaviour of duplex stainless steel is very close to that of a rigid surface. This is consistent with the observation of delay in pressure peaks and lower magnitude of impact pressures on compliant coatings. It will probably be difficult to compare the results of this study with experiments, given the small sizes involved. However we believe that our numerical technique and the results presented in this paper can give useful insights. The developed solvers and methodology can be extended to predict cavitation dynamics in complex flow applications.

The two-way coupled simulations do provide more reasonable predictions of pressure loadings on deformable solid walls as well as the plasticity generated due to loading in the solid. The behaviour of the solid wall is assumed to be rigid in one-way FSI and no attenuation of hydrodynamic loads is possible. This is a reliable first approximation and comparatively easier to implement for cases with high magnitude impact loads in comparison to yield strength, and for harder materials, for example stainless steel or alloys used in industrial applications. On the other hand, if the solid wall displacement is large, a two-way coupling approach is needed to account for the feedback of the solid wall displacement into the fluid domain. Such an analysis is required when the impact pressure loads are closer to the material yield strength (where a slight change in pressure loading can generate large changes in plastic strain development), or for compliant, visco-elastic materials. Therefore, based on the material response from one-way coupling, the need for a two-way coupled fluid-structure interaction can be evaluated for a given material.

Acknowledgement

This research work was accomplished within the project CaFE [3] which has received funding from the European Union Horizon 2020 Research and Innovation programme, Grant Agreement No 642536 under the Marie Skłodowska-Curie Innovative Training Network. We are grateful for this support.

References

Beattie, D., Whalley, P., 1982. A simple two-phase frictional pressure drop calculation method. International journal of multiphase flow 8, 83–87.

Best, J., Kucera, A., 1992. A numerical investigation of non-spherical rebounding bubbles. Journal of fluid mechanics 245, 137–154.

Blake, J., Gibson, D., 1987. Cavitation bubbles near boundaries. Annual Review of Fluid Mechanics 19, 99–123.

3. http ://cafe-project.eu

Chahine, G., Hsiao, C.T., 2015. Modelling cavitation erosion using fluid-material interaction simulations. Interface Focus 5.

Chnafa, C., Mendez, S., Nicoud, F., 2014. Image-based large-eddy simulation in a realistic left heart. Computers & Fluids 94, 173–187.

Cook, A., Cabot, W., 2004. A high-wavenumber viscosity for high-resolution numerical methods. Journal of Computational Physics 195, 594–601.

Di Paola, F., Guerin, C., Berthinier, C., Paredes, R., 2017a. Starting with cast3m thermo-mechanical calculations - training manual.

Donea, J., Huerta, A., Ponthot, J.P., Rodríguez-Ferran, A., 2004. Arbitrary Lagrangian–Eulerian Methods. American Cancer Society. chapter 14.

Dular, M., 2006. Experimental and numerical modeling of cavitation erosion. Sixth International Symposium on Cavitation, CAV2006 .

Egerer, C., Hickel, S., Schmidt, S., Adams, N., 2013. Les of turbulent cavitating shear layers, in : High Performance Computing in Science and Engineering '13. Springer, pp. 349–359.

Fivel, M., Franc, J.P., Roy, S., 2015. Towards numerical prediction of cavitation erosion. Interface focus 5, 20150013.

Fortes-Patella, R., Reboud, J., Briancon-Marjollet, L., 2004. A phenomenological and numerical model for scaling the flow aggressiveness in cavitation erosion, in : EROCAV Workshop, Val de Reuil, France, pp. 283–290.

Franc, J.P., 2009. Incubation time and cavitation erosion rate of work-hardening materials. Journal of Fluids Engineering 131, 021303.

Gong, K., Shao, S., Liu, H., Wang, B., Tan, S.K., 2016. Two-phase sph simulation of fluid–structure interactions. Journal of Fluids and Structures 65, 155–179.

Hirt, C., Amsden, A., Cook, J., 1974. An arbitrary lagrangian-eulerian computing method for all flow speeds. Journal of computational physics 14, 227–253.

Joshi, S., Franc, J.P., Ghigliotti, G., Fivel, M., 2019. Sph modelling of a cavitation bubble collapse near an elasto-visco-plastic material. Journal of the Mechanics and Physics of Solids 125, 420–439.

Kraushaar, M., 2011. Application of the compressible and low-Mach number approaches to Large-Eddy Simulation of turbulent flows in aero-engines. Ph.D. thesis. Institut National Polytechnique de Toulouse-INPT.

Kumar, J., Wurm, F.H., 2015. Bi-directional fluid–structure interaction for large deformation of layered composite propeller blades. Journal of Fluids and Structures 57, 32–48.

Lauterborn, W., Ohl, C.D., 1997. Cavitation bubble dynamics. Ultrasonics sonochemistry 4, 65–75.

Lauterborn, W., Vogel, A., 2013. Shock wave emission by laser generated bubbles, in : Bubble dynamics and shock waves. Springer, pp. 67–103.

Malandain, M., 2013. Simulation massivement parallèle des écoulements turbulents à faible nombre de Mach. Ph.D. thesis. INSA de Rouen.

Moureau, V., Bérat, C., Pitsch, H., 2007. An efficient semi-implicit compressible solver for large-eddy simulations. Journal of Computational Physics 226, 1256–1270.

Paquette, Y., 2017. Interaction Fluide-Structure et Érosion de Cavitation. Ph.D. thesis. Université Grenoble Alpes.

Plesset, M., Chapman, R., 1971. Collapse of an initially spherical vapour cavity in the neighbourhood of a solid boundary. Journal of Fluid Mechanics 47, 283–290.

Pöhl, F., Mottyll, S., Skoda, R., Huth, S., 2015. Evaluation of cavitation-induced pressure loads applied to material surfaces by finite-element-assisted pit analysis and numerical investigation of the elasto-plastic deformation of metallic materials. Wear 330, 618–628.

Poinsot, T., Lele, S., 1992. Boundary conditions for direct simulations of compressible viscous flows. Journal of computational physics 101, 104–129.

Popinet, S., Zaleski, S., 2002. Bubble collapse near a solid boundary : a numerical study of the influence of viscosity. Journal of Fluid Mechanics 464, 137–163.

Roy, S., Franc, J.P., Fivel, M., 2015. Cavitation erosion : Using the target material as a pressure sensor. Journal of Applied Physics 118, 164905.

Roy, S., Franc, J.P., Pellone, C., Fivel, M., 2015a. Determination of cavitation load spectra-part 1 : Static finite element approach. Wear 344, 110–119.

Sarkar, P., 2019. Simulation of cavitation erosion by a coupled CFD-FEM approach. Ph.D. thesis. LEGI, Universite Grenoble Alpes.

Silverrad, D., 1912. Propeller erosion. Engineering 33.

Tijsseling, A.S., Vardy, A.E., 2005. Fluid–structure interaction and transient cavitation tests in a t-piece pipe. Journal of Fluids and Structures 20, 753–762.

Tinguely, M., 2013. The effect of pressure gradient on the collapse of cavitation bubbles in normal and reduced gravity. Ph.D. thesis. Laboratoire de Machines Hydrauliques.

Tong, R., Schiffers, W., Shaw, S., Blake, J., Emmony, D., 1999. The role of 'splashing' in the collapse of a laser-generated cavity near a rigid boundary. Journal of Fluid Mechanics 380, 339–361.

Vantieghem, S., 2011. Numerical simulations of quasi-static magnetohydrodynamics using an unstructured finite-volume solver : development and applications. Ph.D. thesis. Universite Libre de Bruxelle.

Wang, Q., Blake, J., 2010. Non-spherical bubble dynamics in a compressible liquid. part 1. travelling acoustic wave. Journal of Fluid Mechanics 659, 191–224.